Geophys. J. Int. (1996) **127**, 492–502

Wave propagation in a multiple-scattering upper mantle—observations and modelling

M. Tittgemeyer,[1] F. Wenzel,[1] K. Fuchs[1] and T. Ryberg[2]

[1] *Geophysical Institute, University of Karlsruhe, Hertzstrasse* 16, D-76187 *Karlsruhe, Germany*

[2] *GeoForschungsZentrum Potsdam, Telegrafenberg* A3, D-14473 *Potsdam, Germany*

Accepted 1996 July 19. Received 1996 June 17; in original form 1995 August 18

SUMMARY

A striking feature of Russian long-range seismic refraction data from Peaceful Nuclear Explosions is the observation of a high-frequency teleseismic P_n phase, which travels with a group velocity of 8.0 km s^{-1} out to distances of several thousands of kilometres. Modelling using the reflectivity method shows that this phase can be understood as the response of an upper mantle that contains random RMS velocity fluctuations of about ± 4 per cent superimposed on a positive velocity gradient. This class of model explains the existence of the teleseismic P_n, its high-frequency content and its coda length. A teleseismic P_n can only be generated if velocity fluctuations are strong enough to cause multiple scattering and occur on a subwavelength scale. Cross-correlation properties of P- and S-wave velocity fluctuations exert a substantial influence on the wavefield. A completely unexpected phase can be observed if the fluctuations are imposed on a negative gradient

Key words: inhomogeneous media, layered media, scattering, seismic refraction, upper mantle, wave propagation.

INTRODUCTION

Recent observations on long-range refraction data from the Russian seismological Peaceful Nuclear Explosion (PNE) programme between 1971 and 1990 indicate the existence of the so-called teleseismic P_n phase, which travels within the upper-mantle lithosphere to observational distances of several thousands of kilometres (Ryberg *et al.* 1995). This phase could be clearly identified on the shots of the PNE profile QUARTZ. It is also visible in data from the Early Rise experiment (Hales 1972). The notation teleseismic P_n has been used previously by Molnar & Oliver (1969), who investigated efficient long-range propagation of mostly S_n waves generated by earthquakes. Those waves could be observed to travel with upper-mantle velocities for several thousands of kilometres and are reported as high-frequency signals, both for continental and oceanic paths. Unfortunately, the sparseness of the net of earthquake stations did not allow seismic sections to be plotted, and thus the evolution of the teleseismic P_n with distance cannot be visualized.

As a likely explanation for the efficient propagation of the P_n, several authors consider the existence of a sub-Moho waveguide. For this waveguide several theories have been proposed: transmission of energy as a whispering-gallery wave multiply reflected at the crust–mantle boundary (Menke & Richards 1980); transmission of energy in a high-velocity layer beneath the Moho as 'lid' and normal modes (Stephans & Isacks 1977; Mantovani *et al.* 1977); transmission of energy in a low-velocity zone beneath the Moho (Sutton & Walker 1972); tunnelling of low-frequency waves through thin high-velocity layers (Fuchs & Schulz 1976); transmission of energy by reverberations within the lithosphere, the crust and (in the marine case) the water column (Gettrust & Frazer 1981; Sereno & Orcutt 1985, 1987); and propagation in models containing random velocity fluctuations in the crust and/or upper mantle (Menke & Chen 1984; Richards & Menke 1983). Simulations of the wave propagation in analog seismic models of scattering earth structure (Menke & Richards 1983) show that layers of scatterers within the mantle could explain, in certain respects, the coda phenomenon of the teleseismic P_n phase.

Although many theories have been advanced, no commonly accepted mechanism for the explanation of this efficient waveguide exists. Ryberg *et al.* (1995) showed that a waveguide, which is generated by random successions of high- and low-velocity layers, can quantitatively explain the main features of the teleseismic P_n as observed on profile QUARTZ, such as coda length, frequency enhancement and group velocity. In this paper we wish to address fundamental questions regarding this class of model.

(1) How can a high-frequency P_n phase be generated that arrives at teleseismic distances after a low-frequency refracted first-arrival wave?

(2) If we assume a scattering model as being responsible for the P_n phenomena, do we need multiple scattering to explain the observations in the upper mantle or is single scattering sufficient?

(3) What kind of spatial distribution or correlation properties of random velocity fluctuations is needed in order to explain the generation of the teleseismic P_n phase, its frequency content and its coda length?

Unfortunately, there is no theory available that predicts post-critical wave propagation in thinly layered media. Most of the available work refers to near-vertical transmission studies, such as the O'Doherty–Anstey formula (O'Doherty & Anstey 1971) in exploration seismology or recent attempts to extend this theory to subcritical reflections (Burridge *et al.* 1993; Shapiro, Zien & Hubral 1994; Shapiro & Hubral 1996). We therefore have to apply numerical modelling techniques in order to understand key features of wave propagation for the class of models we believe are relevant to our data. We restrict ourselves deliberately to 1-D modelling with the elastic reflectivity method (Fuchs & Müller 1971). Although upper-mantle structures will vary laterally, we attempt to understand the basic phenomena in a low-parameter model space before trying to proceed to more complex 2-D or even 3-D models.

OBSERVATIONS ON PNE PROFILES

The data analysed for the high-frequency teleseismic P_n phase belong to the system of long-range deep seismic sounding profiles carried out by Russian scientists from 1971 to 1990. Peaceful Nuclear Explosions (PNE) and numerous chemical explosions were used as powerful sources. The studies investigated the velocity structure of the crust and upper mantle (Egorkin & Pavlenkova 1981; Egorkin & Chernyshov 1983; Pavlenkova & Egorkin 1983; Egorkin *et al.* 1987). In particular, the seismic data from the QUARTZ profile, located in northern Eurasia (Fig. 1), were used to investigate high-frequency teleseismic P_n. About 400 short-period (1–2 Hz) three-component analogue recording systems were deployed to record the ground motion, resulting in maximum observation distances of about 3200 km. The average station spacing of about 10 km along the profiles provides a unique data density for studies of teleseismic P_n.

The recorded wavefield of the three main shots on the QUARTZ profile shows distinct phases that are associated with the large-scale velocity structure of the crust and upper mantle. Recent studies on the velocity structure below northern Eurasia show remarkable lateral inhomogeneities in the crust and upper mantle (Egorkin & Mikhaltsev 1990; Mechie *et al.* 1993; Ryberg *et al.* 1996).

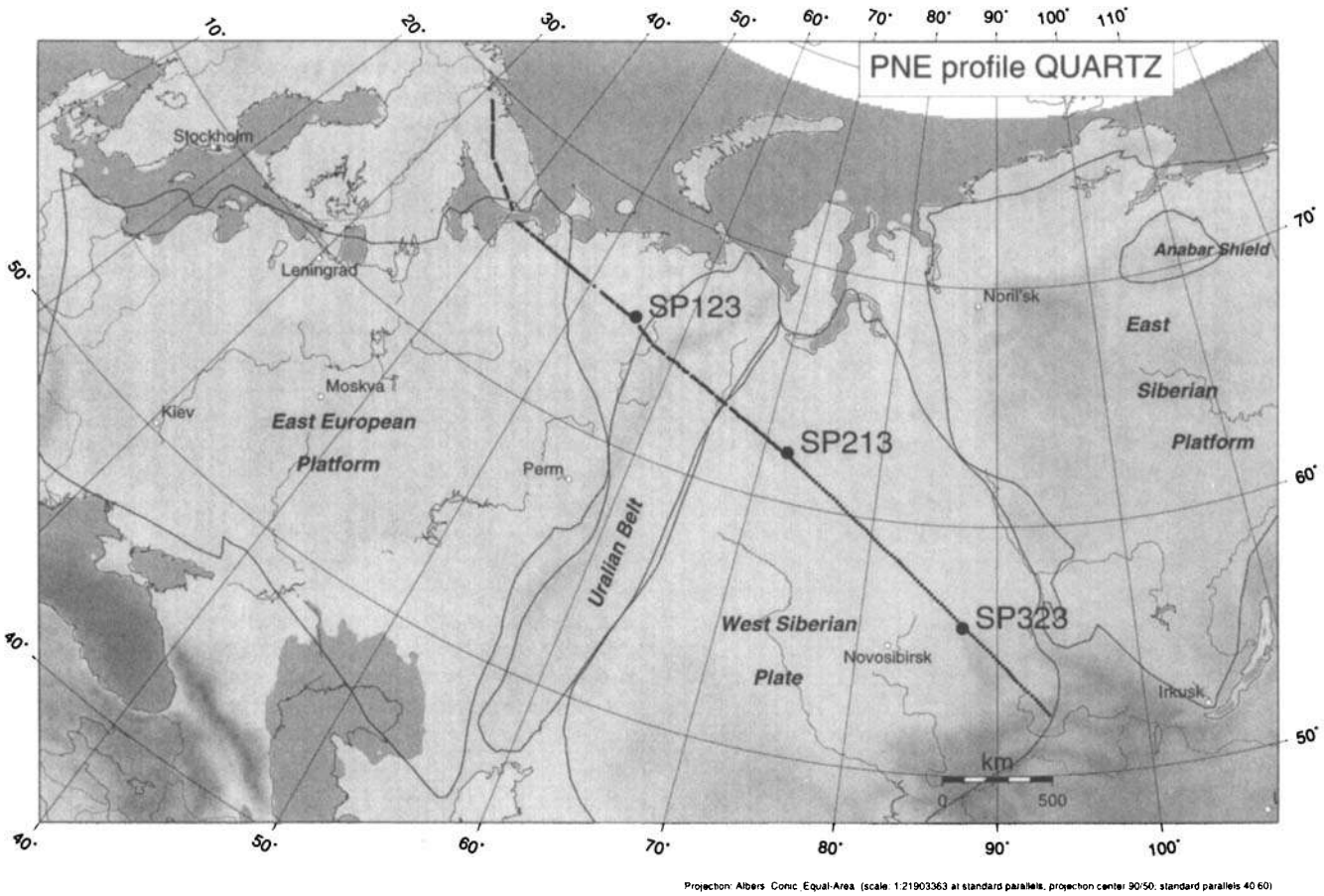

Figure 1. Map of northern Eurasia with the profile QUARTZ (heavy dotted line). Major tectonic provinces are indicated. The three shotpoints (filled circles) for the profile QUARTZ are indicated by their official code. The station spacing on the line was about 10 km. Numerous interspersed chemical explosions provide crustal control. The projects were managed by GEON, the geophysical exploration unit of the Ministry of Geology of the former USSR.

In addition to these distinct phases, the high-frequency part of the wavefield differs strongly from the corresponding low-frequency constituent. Ryberg *et al.* (1995) show that it is clearly dominated by teleseismic P_n (Fig. 2), defined as a phase that travels with a group velocity of 8.1 km s^{-1} and has no sharp first onset. At distances greater than 1300 km it arrives after the wave diving through the upper mantle. As shown by Ryberg *et al.* (1995) this phase contains only high-frequency energy, in the bandwidth 5–12 Hz, and is characterized by a long incoherent coda.

MODELLING UPPER-MANTLE WAVEGUIDES

In modelling the upper-mantle waveguide we use a standard crustal structure. It consists of a homogeneous upper and lower crust with *P*-wave velocities of 5.8 km s^{-1} for the upper crust and 6.5 km s^{-1} for the lower crust between 20 and 35 km depth. The Moho is marked by a first-order discontinuity at 35 km depth. The upper 75 km of the mantle are characterized by a gradient zone. This could be either slightly positive or negative. For this zone we apply a constant frequency-independent Q_p of 1400 and a constant frequency-independent Q_s of 600.

Model 1 (Fig. 3) containing a positive gradient serves as a reference for Models 2 to 6, where random fluctuations of elastic parameters are superimposed on the upper-mantle gradient. Numerically we generate these fluctuations with a series of random numbers representing white noise with a given standard deviation. The series is then convolved with an exponential function (autocorrelation function) so that the statistical quantity describing the average layer thickness of the medium is the correlation length.

Below a depth of 120 km the gradient structure with or without fluctuations is followed by a half-space with constant velocity. In real-Earth seismograms the response from the upper-mantle transition zones could interfere with the wavefield shown in the figures. Again, to see the effects of the uppermost mantle as clearly as possible, we omit these waves by assuming a half-space beneath 120 km depth. We distinguish two possible fluctuations of elastic parameters. (1) The case where only the *P*-wave velocity fluctuates and the *S*-wave velocity does not. In other words, the *P*-wave velocity variations are accompanied by variations in Poisson's ratio. (2) The case where *P*- and *S*-wave velocities both vary, according to a correlation coefficient of 1, so that Poisson's ratio remains constant. Computations with variable options for the densities indicate that the class of synthetic seismograms we consider is insensitive to this parameter for distances beyond the critical point of P_MP. For this reason the density was simply kept constant. The models shown in the figures represent the flat-earth analogue model for which the seismograms are computed. In order to observe these seismograms on a curved earth, the velocity models as shown in the figures have to be transformed according to the flat-earth transformation rules (Müller 1971). As a rule of thumb this would result in a reduction of velocities by 0.04 km s^{-1} at the Moho depth and by 0.15 km s^{-1} at 120 km depth. All synthetic seismograms represent the vertical

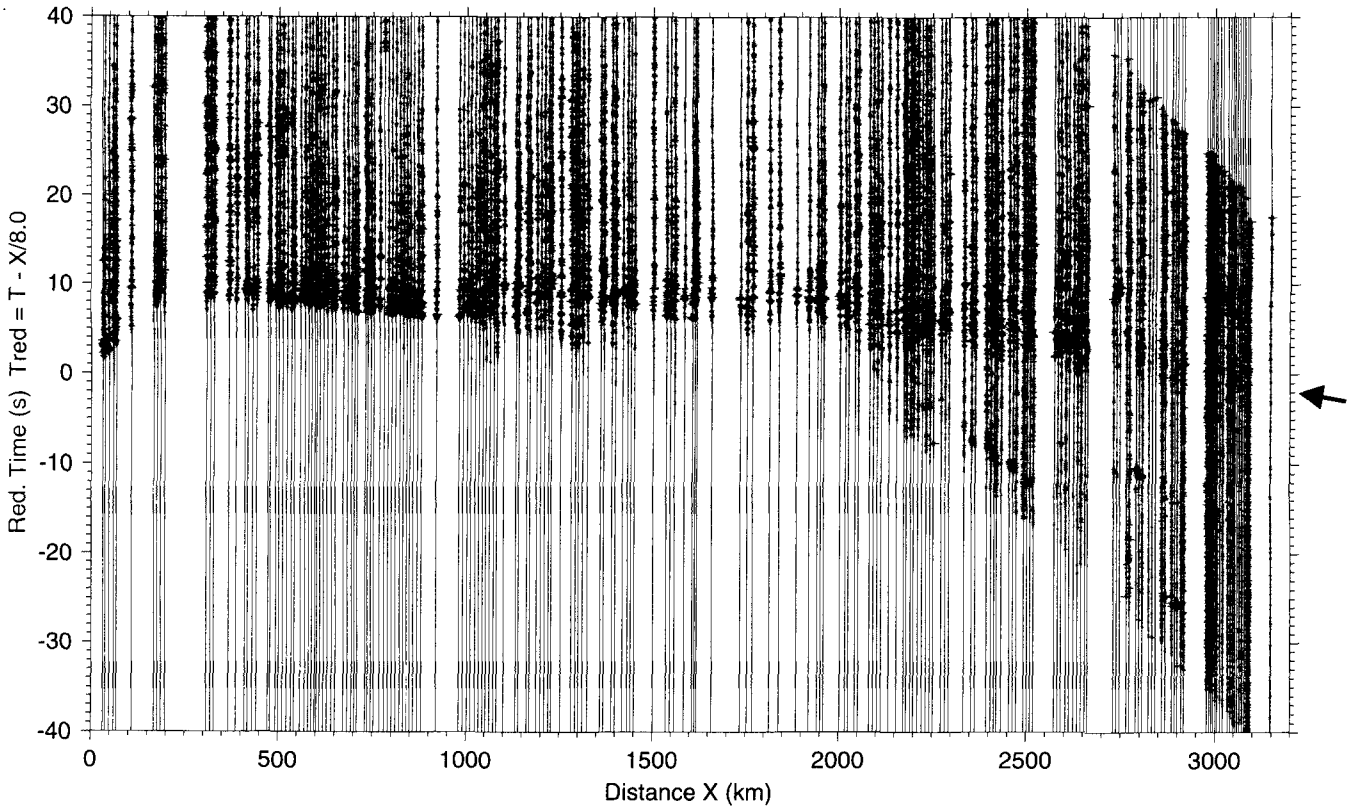

Figure 2. High-pass filtered (corner frequency $f = 5$Hz) vertical-component time–distance record section (reduction velocity 8.0 km s^{-1}) on profile QUARTZ for shotpoint 323 recorded to the northwest. It is trace-normalized individually to maximum trace amplitude. The marked strong waveband (arrow) travelling with a group velocity of 8.1 km s^{-1} is the high-frequency teleseismic P_n.

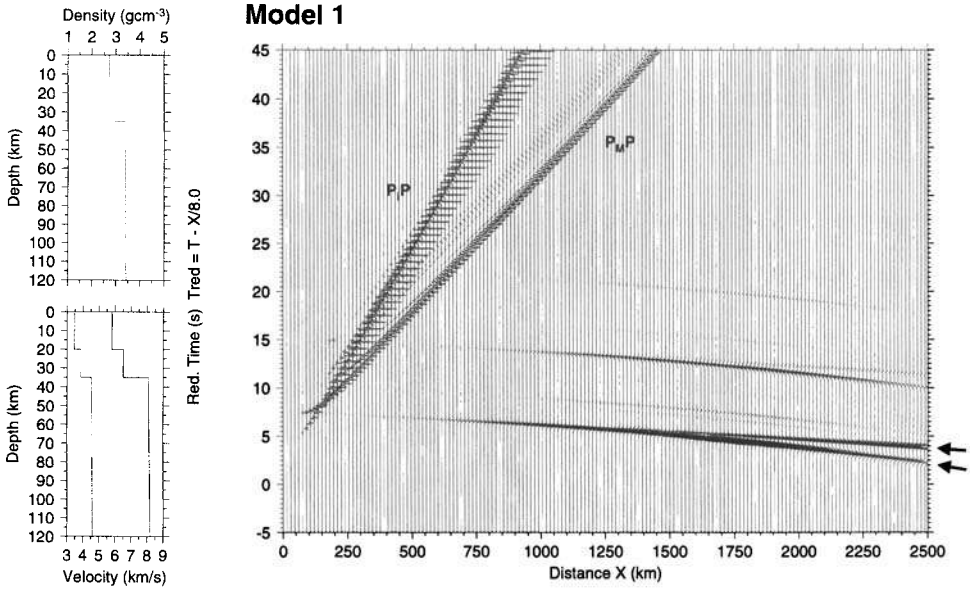

Figure 3. *P*-wave theoretical record section calculated with the reflectivity method for Model 1. True amplitudes of the vertical component are displayed with an offset-dependent gain factor $10^{-4} \times \text{offset}^{3.0}$. The reduction velocity is 8.0 km s^{-1}. The velocity–depth functions and the density–depth function that Model 1 is based on are plotted to the left. The model contains an upper and a lower crust, a step-like Moho and a small upper-mantle gradient of 0.001 km s^{-1} km^{-1}. Note that the wave diving into the upper mantle splits into two phases, the direct wave (fast) and the first whispering-gallery refraction (slow arrival).

component. The duration of the source signal was 25 ms for all of the synthetic seismograms, which results in a dominant frequency of ~4 Hz. They are computed and shown for an offset range of 0 to 2500 km. For all displays the time is reduced by offset/8.0 km s^{-1}, and synthetic seismograms are displayed with an offset-dependent gain factor of $10^{-4} \times \text{offset}^{3.0}$. All synthetics are thus comparable in a true-amplitude sense.

MODEL 1 (FIG. 3)

Fig. 3 shows the synthetic seismograms for Model 1. It contains only an upper and lower crust, a step-like Moho and a small upper-mantle gradient of 0.001 km s^{-1} km^{-1}. The shear-wave velocity is set to 4.5 km s^{-1} at the Moho depth; the density is determined by the Birch (1961) relation. Not only can the Moho reflection and the wave diving into the upper mantle be seen, but also their respective multiple and converted waves generated at the free surface and the Moho. The mantle refraction remains weak between the critical distance of P_MP and 750 km. It splits into two phases, the fast phase being the direct diving wave and the slow arrival representing the first branch of the whispering-gallery Moho reflection. As expected, no feature like the teleseismic P_n with its incoherent coda is visible. Model 1 and its seismograms serve as a reference for the next models, which include mantle fluctuations.

MODEL 2 (FIG. 4)

In Model 2, random *P*-wave velocity fluctuations with a variance of ± 0.4 per cent are superimposed on the upper-mantle structure of Model 1 whilst the *S*-wave velocities and densities remain unchanged. We observe several distinct differences in comparison to the wavefield of Model 1 (Fig. 3).

(1) The first breaks are followed by a short coda of 4 to 5 s length increasing towards larger offsets. A potential whispering-gallery phase is hidden in the coda.

(2) At a distance of 2500 km, the first arrival in Fig. 4 is little lower in frequency than in Fig. 3, an effect that is related to the tunnelling of the refracted wave on its path through the high-velocity layers that exceed the average velocity. Evidently this is not the dominant effect and should emerge strongly if the variance of fluctuations increases. We discuss this in the next section.

(3) Amplitudes of the refracted wave in Fig. 4 are high. At a given distance there is clearly more energy returned to the surface than with a simple gradient. This observation applies in particular to small distances. Despite these differences, the wavefield of Model 2 can be viewed as a perturbation of the wavefield produced by Model 1: the weak fluctuations result in a diving mantle wave, with a short coda appended; neither conspicuous frequency effects nor the generation of a teleseismic P_n can be observed.

(4) The appearance of subcritical primary and multiple reflections from the fluctuations on hyperbola-type traveltime branches.

MODEL 3 (FIG. 5)

Here we superimpose stronger fluctuations (±4 per cent) than in Model 2. Again, only the *P*-wave values vary randomly. This model results in a qualitative change in the emerging wavefield (Fig. 5). First of all a teleseismic P_n phase travelling at 8.0 km s^{-1} is generated. This phase is not a distorted refraction but rather a new phase, which arises from the composite properties of strong scattering. It travels with a velocity distinctly different from that of the whispering-gallery phase, as indicated by a comparison of Figs 4 and 5. The teleseismic P_n is preceded from distances of 1000 km and

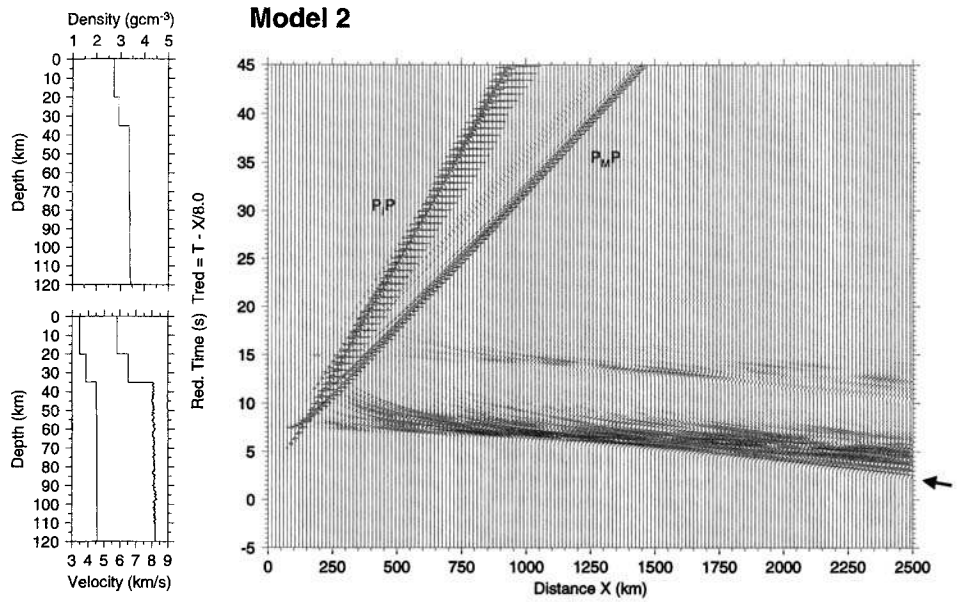

Figure 4. *P*-wave theoretical record section calculated with the reflectivity method for Model 2. In order to facilitate comparison with the other models, true amplitudes for the vertical component are displayed with an offset-dependent gain factor of $10^{-4} \times \text{offset}^{3.0}$. The reduction velocity is 8.0 km s^{-1}. The velocity–depth functions and the density–depth function that Model 2 is based on are plotted to the left. Model 1 serves as a reference background model. On the upper-mantle *P*-wave velocity gradient, fluctuations are superimposed that are characterized by a variance of $\pm$ 0.4 per cent and a correlation length of 500 m. The sampling rate for the fluctuations is 0.1 km, which implies that the model in that range consists of 750 homogeneous layers. Note that the first breaks are tailed by a short coda. A potential whispering-gallery wave is hidden in the coda.

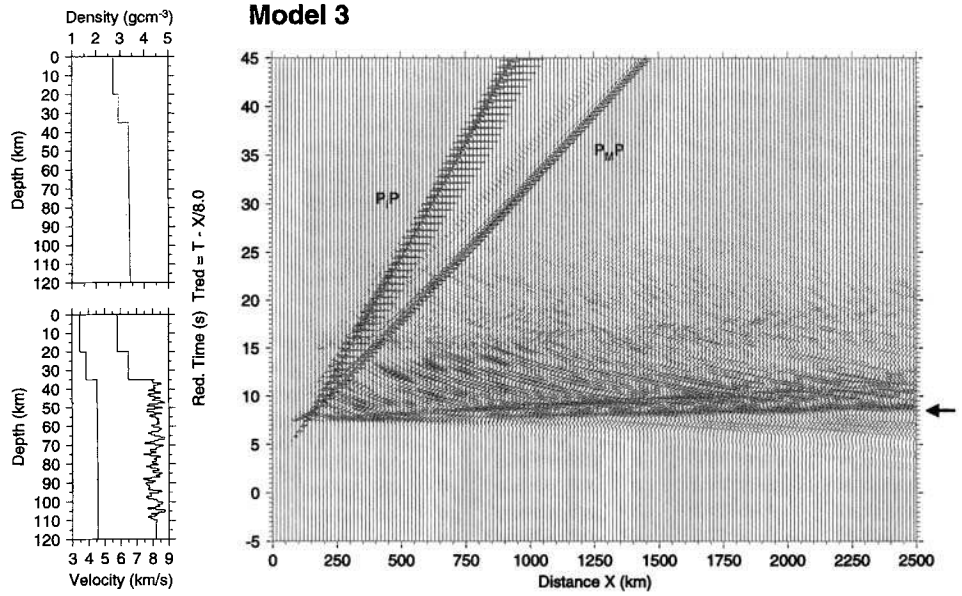

Figure 5. *P*-wave theoretical record section calculated with the reflectivity method for Model 3. True amplitudes for the vertical component are displayed with an offset-dependent gain factor of $10^{-4} \times \text{offset}^{3.0}$ in order to facilitate comparison with the other models. The reduction velocity is 8.0 km s^{-1}. The velocity–depth functions and the density–depth function that Model 3 is based on are plotted to the left. Model 1 serves as a reference background model. Compared with Model 2, the *P*-wave velocity fluctuations that are superimposed on the positive upper-mantle gradient are stronger ($\pm$ 4 per cent). The correlation length is 2 km. Note that a teleseismic P_n is generated, which is characterized by a group velocity of 8.0 km s^{-1} and an extensive coda.

farther) by the refracted wave, which dives through the medium with something like the average velocity of the gradient. This wave is low frequency, which is related to the fact that on its path on an averaged gradient it has to tunnel through all the high-velocity layers that exceed the average velocity. As low-frequency waves tunnel more easily than high-frequency waves (Fuchs & Schulz 1976), this phase progressively loses high frequencies along its path. On the other hand, the high-frequency portions of the wavefield that penetrate beneath the Moho are returned to the surface and become part of the teleseismic P_n and its coda, which therefore turns into a high-frequency phase.

The teleseismic P_n is characterized by a group velocity of about 8.0 km s^{-1} and an extensive coda. It is not at all obvious why and how this phase is generated. The low-frequency refraction could be expected from the well-known tunnel effect in supercritical wave propagation. We expect that the refraction is tailed by a coda, which should be longer than in Fig. 4 because of the more intense scattering. It is extremely important to note that, instead, a qualitative new feature arises if scattering becomes more intense. This is not just more scattering into the coda or more attenuation and loss of coherence in the first arrival, but is a new phase—the teleseismic P_n.

Also, the synthetics of Model 3 indicate that the fluctuations generate a supplementary effect. The arrival time of the first breaks increases moderately. This implies that the kind of fluctuation we impose on the gradient decreases the effective velocity for refracted waves by about 1 per cent. It is not surprising that this effect occurs. For subcritical wave propagation it has been established that elastic waves 'feel' subwavelength structures such that the medium adopts effective velocities. For post-critical propagation no appropriate theory has been developed. Even so, the effect is quite obvious in our synthetic seismograms.

We use the differences in wavefield characteristics to define weak and strong scattering for supercritical wave propagation. In Fig. 4 scattering only modifies the wavefield that would propagate without fluctuations and is therefore called weak. Increasing the fluctuations creates new features of the wavefield and scattering is therefore called strong. We want to emphasize that this is a purely phenomenological definition. Scattering describes properties of the wavefield as they emerge in a fluctuating medium. Given a certain variance of the elastic parameters and a certain dominant wavelength of a transmitted wave, the observation of weak or strong scattering depends on the travelpath. For long paths scattering is always strong. Increasing the variance of the fluctuations will shift the distance that separates weak and strong scattering towards smaller offsets (Shapiro & Kneib 1993).

MODEL 4 (FIG. 6)

This model again contains ± 4 per cent P-wave velocity fluctuations superimposed on the positive upper-mantle gradient. It differs from Model 3 by the correlation length of the random fluctuation. Whereas Model 3 is characterized by a correlation length of 2 km, we use a length of 3.5 km in Model 4. More intuitively speaking, the fluctuations are of longer wavelengths, although the velocity contrasts are about the same as in Model 3. The synthetics of Fig. 6 indicate that if the correlation distance is not sufficiently small, the wavefield becomes diffuse and cannot be interpreted in term of phases. No coherent first arrival can be correlated along more then a few kilometres. No phase travelling with the velocity of the averaged gradient can be identified. First arrivals are short traveltime branches of refractions from the high-velocity teeth, which rapidly break down in amplitude. It is notable that no teleseismic P_n is formed. The synthetics of this model show that an appropriate small correlation length of the random fluctuations of the upper mantle is needed in order to form a wavefield, which can be characterized by coherent seismic phases. It can be expected that a finite length of lamellae will exert a strong influence on the wavefield. Quantitative statements, however, are not yet possible.

Although Model 4 obviously cannot satisfy our observations on QUARTZ, it is indicative of how teleseismic P_n may be generated. As the model contains only a few high-velocity teeth, the individual reflections and their multiples from those teeth are clearly visible. We are convinced that the superposition of many branches of supercritical reflections and their multiples from those teeth constructively interfere to form the teleseismic P_n. They are thus able to build up a group velocity that is less than the velocity of the average gradient. The contrast with the high-velocity teeth determines the critical angle, which in turn controls where along the individual traveltime curve the amplitudes become critical and thus strong. The superposition of all the individual reflections results in a band of high amplitudes following the phase arrival. The length of this band is controlled by the velocity contrast with the high-velocity teeth.

MODEL 5 (FIG. 7)

This model is identical to Model 3, apart from the fact that the S-wave velocities fluctuate too, in other words the Poisson ratio is kept constant at 0.25. The synthetics of Fig. 7 show that the main features of the wavefield of Model 3 (Fig. 5) are conserved. However, the teleseismic P_n loses spatial coherency and appears to emerge as an envelope of spatially limited wave packets. In addition, the coda is shorter than in Model 3. Model 5 indicates that for a quantitative estimate of the coda properties the statistical characteristics of P- and S-wave fluctuations are equally important. This can be viewed as a favourable characteristic because it will allow P- and S-velocity variations to be constrained and thus will provide a much better indication of the compositional properties of the upper mantle, which ultimately cause this type of elastic structure.

MODEL 6 (FIG. 8)

The results discussed so far demonstrate that strong random velocity fluctuations can do more than just distort a phase: they can generate a new phase. This encouraged us to extend the class of upper-mantle models by superimposing fluctuations on a negative gradient. Therefore, in this model velocity fluctuations with the same variance and correlation length as specified for Model 3 are superimposed on a negative upper-mantle gradient. The result (Fig. 8) is quite surprising. There is no refracted wave as in Model 3 because of the negative gradient. On the other hand, a teleseismic P_n is still formed, now travelling with a velocity of about 7.9 km s^{-1}. As will be discussed in the next section, this phase can still be explained using the scheme of constructive interference of post-critical reflections and their multiples. As the refracted phase is lacking, no separation of energy in low- and high-frequency portions as in Fig. 5 occurs. The tunnel effect may still play a role, but with a less obvious result because the low- and high-frequency parts of the wavefield are mixed up in the coda following the first breaks. Therefore, the teleseismic P_n is not characterized by particularly high frequencies. An interesting implication of the model becomes obvious if we try to interpret the synthetics in the classical way. Only interpreting the first arrivals, one would conclude that the upper mantle underneath the Moho has a velocity of 7.9 km s^{-1} and that a positive gradient prevails because the phase can be traced out to large distances. The interpretation would be in strong contrast to the truth,

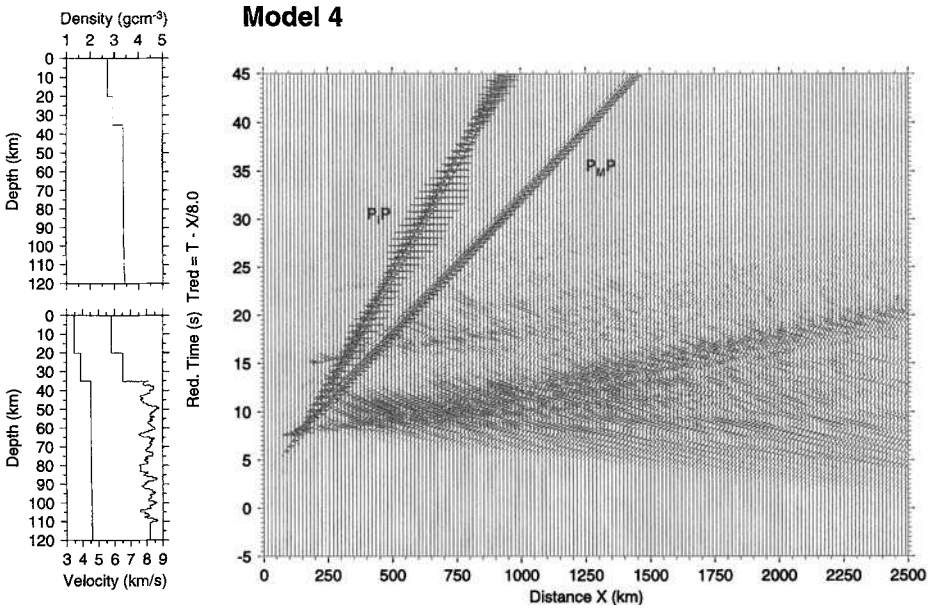

Figure 6. *P*-wave theoretical record section calculated with the reflectivity method for Model 4. True amplitudes for the vertical component are displayed with an offset-dependent gain factor of $10^{-4} \times \text{offset}^{3.0}$ in order to facilitate comparison with the other models. The reduction velocity is 8.0 km s^{-1}. The velocity–depth functions and the density–depth function that Model 4 is based on are plotted to the left. Model 1 serves as a reference background model. In contrast to Model 3, the correlation length is 3.5 km. *P*-wave velocity fluctuations, which are superimposed on the positive upper-mantle gradient, are ± 4 per cent. As in Model 3, Model 4 consists of 150 homogeneous layers in the region of the gradient zone. Note that the wavefield has become more diffuse (compare with Fig. 5) and is not able to be interpreted in term of phases.

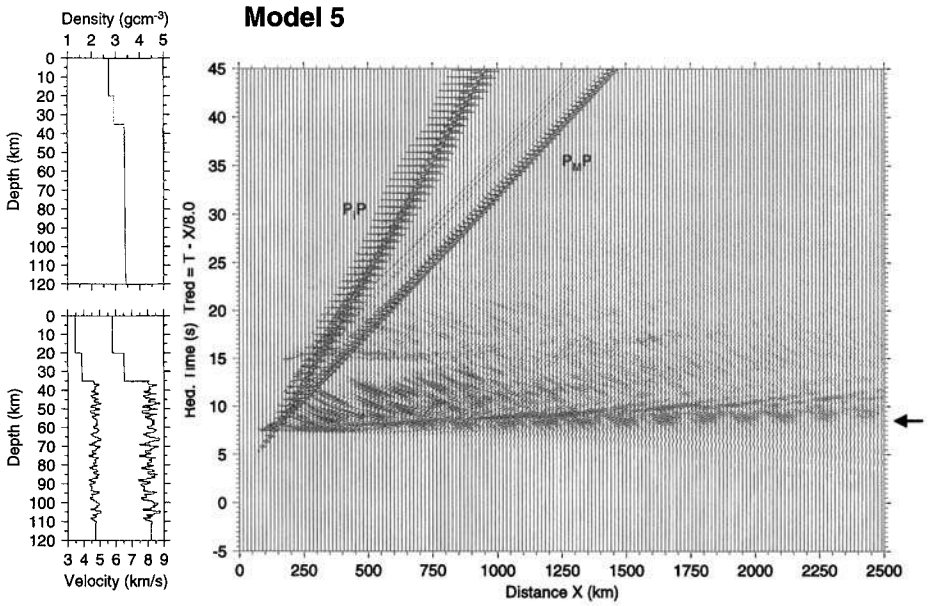

Figure 7. *P*-wave theoretical record section calculated with the reflectivity method for Model 5. True amplitudes for the vertical component are displayed with an offset-dependent gain factor of $10^{-4} \times \text{offset}^{3.0}$ in order to facilitate comparison with the other models. The reduction velocity is 8.0 km s^{-1}. The velocity–depth function and the density–depth function that Model 5 is based on are plotted to the left. This model is identical to Model 3, apart from the fact that the *S*-wave velocities fluctuate. The Poisson ratio is therefore kept constant at 0.25. Note that the P_n loses spatial coherence and appears to emerge as the envelope of spatially limited wave packets.

which is a negative gradient with strong fluctuations superimposed.

EXPLANATION FOR THE MAIN OBSERVATIONS

We try to understand the phenomena by using a qualitative theory, which includes three features: (1) multiple wide-angle reflections within the fluctuating layer; (2) the tunnel effect for supercritical wave propagation; and (3) higher-order Born scattering for transmission properties of waves travelling in fluctuating media. With this approach we can understand the following observations: (1) the generation of teleseismic P_n in upper-mantle structures with positive and negative velocity gradients (2) the high-frequency content of P_n if the gradient is positive; and (3) the length of the

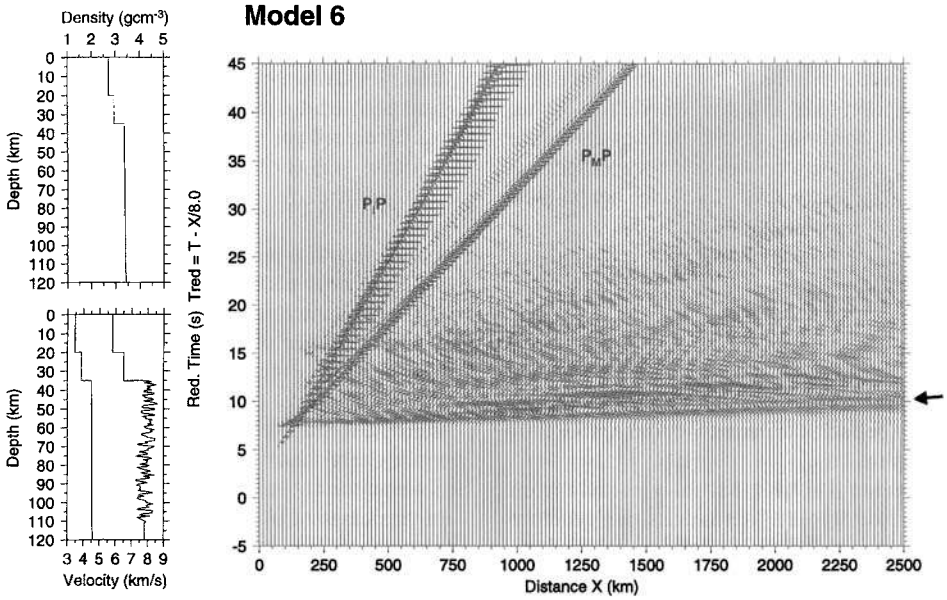

Figure 8. *P*-wave theoretical record section calculated with the reflectivity method for Model 6. True amplitudes for the vertical component are displayed with an offset-dependent gain factor of $10^{-4} \times \text{offset}^{3.0}$ in order to facilitate comparison with the other models. The reduction velocity is 8.0 km s^{-1}. The velocity–depth function and the density–depth function that Model 6 is based on are plotted to the left. In contrast to Model 3, the *P*-wave velocity fluctuations are superimposed on a negative upper-mantle gradient of -0.005 km s^{-1} km^{-1}. The statistical quantities describing the velocity fluctuations are the same as defined for Model 3. It is remarkable that a teleseismic P_n is still formed, now travelling with a velocity of 7.9 km s^{-1}.

associated coda, again for positive and negative upper-mantle gradients.

The seismograms of Model 2 (Fig. 4), which contains the weakly fluctuating upper mantle, indicate that even in this case multiple wide-angle reflections within the scattering zone play an important role in making up the coda. Although relatively short, it cannot be explained by first-order scattering from the inhomogeneities, nor can it be explained by first-order scattering plus multiple (whispering-gallery) reflections from the Moho. At large offsets, traveltime curves for these types of waves all came much too close to the first arrivals to explain the 4 to 5 s of coda seen in Fig. 4. The two other phenomena are almost invisible in the case of Model 2. We cannot see a conspicuous separation into lower and higher frequencies as expected for substantial tunnelling, nor is the first arrival in Fig. 4 delayed by more than a few milliseconds compared to Fig. 3.

A delay effect is caused by dense fluctuations of the medium, which eventually transform it into an 'effective medium'. It is known (Burridge *et al.* 1993; Shapiro *et al.* 1994; Shapiro & Hubral 1995) that wave propagation in an elastic fluctuating medium can be described by an effective medium that is dispersive, anisotropic and shows attenuation. The traveltime curve for a reflection is then defined by the propagation time of a finite-frequency wave. Every wavelet that is defined by a dominant finite frequency arrives later than the (infinite-frequency) traveltimes predict. Dispersion, however, is generally not strong enough to show discernible effects within the limited bandwidth of the wavelet. In consequence, reflections are progressively delayed with larger offsets. If reflections are numerous, as in the case of a short correlation length of the fluctuations, an envelope will form and thus build a phase that is slower than the velocity of the gradient. If the correlation length is large, fewer reflections occur and no coherent phase can form as an envelope phenomenon. This creates the difference between the synthetic seismograms of Figs 5 and 6. Those parts of the wavefield that are not backscattered at a given depth level propagate as a diving wave further down. This wave has to overcome many high-velocity teeth, which only allow for tunnelling of the low-frequency portions of the wavefield. Thus the diving wave loses progressively higher frequencies, which necessarily accumulate within the teleseismic P_n.

An increase of the amplitude of velocity variations is expected to manifest itself in three ways. First, an extended coda will arise. Because the coda is the result of multiple scattering within the depth level where the velocity fluctuations occur, higher velocity contrasts will enhance multiple reflections. Second, a further reduction of the effective velocity that controls the onset times of the first breaks should be observed. Third, tunnel effects must start to play a role because the wave travelling with the effective medium velocity encounters numerous high-velocity teeth, where tunnelling and thus frequency separation must occur.

The synthetics of Models 3 and 4 (Figs 5 and 6) demonstrate the effect of multiple scattering in coda generation. One can clearly discern branches of reflection hyperbolae, which become visible once they exceed an apparent velocity of 8.5 to 8.7 km s^{-1}. The traveltimes of these hyperbolae are distinctly different from those of the primary reflections. In addition, many of them are not just multiply reflected at the Moho boundary, but also within the scattering layer. This high degree of coherency in the wavefield is primarily due to the 1-D modelling procedure, and will disappear as soon as laterally less continuous structures are assumed. Also, the data do not show correlations from trace to trace that are comparable with the synthetics. The uncorrelated wavefield, however, could equally well be caused by station site effects.

Models 3 and 4 differ with respect to the correlation length of the fluctuations, rather than with respect to velocity contrasts. The primary and multiple reflection/refraction branches that characterize Fig. 6 terminate roughly where the diving wave in the undisturbed medium would be expected (see Fig. 3). Each traveltime branch can be viewed as waves terminated by an underlying low-velocity zone. The large correlation length of Model 4 results in a structure that consists of a succession of high- and low-velocity teeth thick enough to avoid substantial tunnelling.

A smaller correlation length such as in Model 3 must allow the low-frequency part of the wavefield to see the fluctuating upper mantle as a constant-gradient medium with an effective velocity smaller than the average. The high-frequency part of the wavefield is multiply reflected within the layers, and thus even more strongly delayed.

Fig. 5 is a surprise because it shows that the wavefield from a simple gradient, with superimposed fluctuations, can generate a low-frequency refracted wave plus a high-frequency low-velocity phase. Alternatively, a more diffuse distribution of frequencies with time was expected. Variations of the statistical properties of the medium in comparison with the frequency band of the source pulse will change the picture, and we have not yet undertaken enough modelling to determine precisely the range of parameters for which the phenomenon of teleseismic P_n is defined.

The traveltime envelope of the reflections and their multiples generates the leading part of the teleseismic P_n. The amplitudes of these reflections control the length of the associated coda. The distribution of amplitudes on an individual reflection is determined by the critical point. If the reflection comes from a high-velocity tooth of the random medium, and if the velocity difference between the tooth and the average gradient above it is high, then the critical point on the reflection curve is located at a high apparent velocity or at a small offset. The converse is true if the difference in velocity becomes smaller. High amplitudes can be expected on the individual traveltime curves from this critical point towards larger offsets. Thus, if velocity fluctuations are large, many reflections will occur with an early critical point. With regard to the entire wavefield, this will provide a long coda. Reduction of the variance of fluctuations will shift the critical point on most reflections and thus shorten the coda.

Another surprising result of our modelling is the phase generated by random fluctuations superimposed on a negative velocity gradient (Fig. 8). The wavefield without these reflections is easy to predict. A strong reflection from the crust–mantle boundary will be associated with an almost invisible P_n travelling at 8.0 km s^{-1}. However, as soon as a reflector is attached to the gradient, reflections and their multiples exist. They start at zero offset with an infinite apparent velocity and terminate at a finite offset where the apparent velocity is 8.0 km s^{-1}. Several of these reflections and their multiples again form an envelope, which acts as a wave emerging from the upper mantle. The negative gradient leads to the fact that the critical point on the traveltime curve is coincident with the point where the curve terminates. Therefore, amplitudes are gradually distributed along the traveltime curve and no conspicuous onset of high amplitudes can be defined. As a consequence, the coda is not as clearly defined as in the case of a positive gradient. Another observation in the seismograms of Fig. 8 is the lack of frequency separation effects. This can be easily explained by the fact that a wave travelling through velocity variations imposed on a negative gradient is, apart from a narrow sub-Moho depth interval, subcritical and thus less exposed to tunnel effects such as occur in the case of a positive gradient.

IMPLICATIONS

We have attempted to show that the observations on long-range seismic profiles call for a class of upper-mantle models that are characterized by random velocity fluctuations. If these are in the range of ± 4 per cent, new features in the wavefield, notably teleseismic P_n, arise. We use the evolution of this phenomenon as the definition for strong scattering. The numerical value of ± 4 per cent is clearly related to the 1-D model, and can be expected to change in two or three dimensions. A proper theoretical frame for wave propagation in this class of model that would predict the generation of a new phase does not yet exist, but ought to be developed.

We deliberately do not discuss details of the frequency selection phenomena and details of the coda because we feel that more realistic 2-D or 3-D models could modify quantitative statements considerably. For instance, we would not expect the refracted phase in Model 3 to lose all of its high frequencies by tunnelling. Lamellae with a limited lateral extent will allow some of the high-frequency energy to penetrate to greater depths without tunnelling and therefore without the loss of higher frequencies.

The size of random velocity fluctuations and their correlation lengths have been found to explain the existence of a teleseismic P_n and its coda properties. For a more comprehensive view of the lithosphere, the model of the upper mantle must be compatible with the well-known fact that the Earth's mantle is in general not reflective for high-frequency near-vertical incidence waves. In other words we must design structures that show strong scattering at lower frequencies and for supercritical wave propagation, but weak scattering (compared to the lower crust) at higher frequencies and vertical incidence. In addition to numerical modelling, near-vertical broad-band seismic experiments with low-frequency sources and arrays built of seismometers with not more then 1 s period are mandatory to the study of the fine structural features of the upper mantle.

Because the actual size of the fluctuations will probably change with the dimensionality of the models, we do not wish to discuss petrological implications in a quantitative sense. It is conceivable that the fluctuations represent the preferred orientation of olivine with a random component. We do not anticipate the entire mantle being uniformly oriented in a particular direction. There will be some orientation that results in random fluctuations in the vertical and probably also in the horizontal direction.

If the type of layering we see in PNE data is a more general phenomenon, as speculated by Fuchs (1995) it could be interpreted as a remnant of a disturbed laminar flow pattern underneath the Moho that must be different from material flow in the lower crust. The latter is generally assumed to result in late- to post-orogenic settings where crustal stacking in a high-temperature environment is re-equilibrated by intensive lower-crustal extension, which is ultimately responsible for its observed reflectivity pattern. The upper mantle and lower crust are different in terms of composition, compositional

variety and rheology. The lower crust is assumed to be predominantly mafic, but to contain both mafic and felsic rocks, which allow for high impedance contrasts. The mantle could have a mineralogically more homogeneous composition, but with highly anisotropic material, in particular olivine. Fluctuations caused by anisotropy are pure velocity variations with unchanged densities. This would result in fairly small near-vertical impedance contrasts. Also, mantle material at a given geotherm can yield higher differential stresses than lower-crustal rocks. These differences may result in different scales of vertical layering and horizontal extent of inhomogeneities.

CONCLUSIONS

Long-range PNE data and previous observations lead to the hypothesis that the upper-mantle velocity structure should be defined by a gradient onto which random vertical velocity fluctuations are superimposed. Characteristics of the fluctuations in terms of amplitude and correlation length are determined by the observation of teleseismic P_n. According to our modelling, this phase can only be generated if fluctuations are strong ($\pm$ 4 per cent) and correlated on a subwavelength scale.

Teleseismic P_n and the observed separation of frequencies can be explained by a quantitative theory that includes multiple scattering and tunnelling of supercritical waves. Most surprisingly, a teleseismic P_n is observed even if the fluctuations ride on a negative gradient. The latter observation calls for a critical reinterpretation of derived upper-mantle velocities.

ACKNOWLEDGMENTS

We acknowledge the advice and discussions with our colleagues at the Geophysical Institute, Karlsruhe. In particular we thank S. A. Shapiro for critical remarks and for providing us with his computer programs. We are also grateful to Uwe Enderle and Veronika Wehrle for programming the interface to GMT (Wessel & Smith 1995), which was used to plot the seismogram sections. The digital data for the QUARTZ profile were kindly made available to us by the GEON/Russian Geological Committee within the EUROPROBE cooperation agreement. The Ministry of Education and Research of Germany (BMBF) supported the digitization of the PNE data at GEON. This paper is contribution 560 to the Priority Research Programme 'Stress and Stress Release in the Lithosphere' at the University of Karlsruhe of the Deutsche Forschungsgemeinschaft.

The calculations were performed on HP-Workstations and the CONVEX computer of the Geophysical Institute and on the SNI S600/20 supercomputer of the computer centre, Karlsruhe University. Geophysical Institute Contribution No. 678.

REFERENCES

Birch, F., 1961. The velocity of compressional waves in rocks to 10 kbars, part 2. *J. geophys. Res.*, **66,** 2199–2224.

Burridge, R., de Hoop, M.V., Hsu, K., Le, L. & Norris, A., 1993. Waves in stratified viscoelastic media with microstructure, *J. acoust. Soc. Am.*, **94,** 2884–2894.

Egorkin, A.V. & Chernyshov, N.M. 1983. Peculiarities of mantle waves from long-range profiles, *J. Geophys.*, **54,** 30–34.

Egorkin, V.A. & Mikhaltsev, A.V., 1990. The results of seismic investigations along geotraverses, in *Super-Deep Continental Drilling and Deep Geophysical Sounding,* pp. 111–119, eds Fuchs, K., Kozlovsky Y.A., Krivtsov, A.I. & Zoback, M.D., Springer Verlag, Berlin, Heidelberg, New York.

Egorkin, A.V. & Pavlenkova, N.I., 1981. Studies of mantle structure of U.S.S.R. territory on long-range seismic profiles, *Phys. Earth planet. Inter.*, **25,** 12–26.

Egorkin, A.V., Zuganov, S.K., Pavlenkova, N.I. & Chernyshov, N.M., 1987. Results of lithospheric studies from long-range profiles in Siberia, in *Seismic Studies of the Continental Lithosphere,* eds Asano, S. & Mooney, W.D., *Tectonophysics,* **140,** 29–47.

Fuchs, K., 1995. Scales of structure and processes in the lithosphere, *IUGG XXI General Assembly,* Boulder, CO.

Fuchs, K. & Müller, G., 1971. Computation of synthetic seismograms with the reflectivity method and comparison with observations, *Geophys. J. R. astr. Soc.*, **23,** 417–433.

Fuchs, K. & Schulz, K., 1976. Tunneling of low-frequency waves through the subcrustal lithosphere, *J. Geophys.*, **42,** 175–190.

Gettrust, J.F. & Frazer, L.N., 1981. A computer model study of the propagation of long-range P_n phase, *Geophys. Res. Lett.*, **8,** 749–752.

Hales, A.L., 1972. The travel times of P seismic waves and their relevance to the upper mantle velocity distribution, *Tectonophysics,* **13,** 447–482.

Mantovani, E., Schwab, F., Liao, H. & Knopoff, L., 1977. Teleseismic S_n: a guided wave in the mantle, *Geophys. J. R. astr. Soc.*, **51,** 709–726.

Mechie, J., Egorkin, A.V., Fuchs, K., Ryberg, L., Solodilov, L. & Wenzel, F., 1993. P wave mantle velocity structure beneath northern Eurasia from long-range recordings along the profile Quartz, *Phys. Earth planet. Inter.*, **79,** 269–286.

Menke, W.H. & Chen, R., 1984. Numerical studies of the coda falloff rate of multiply scattered waves in randomly layered media, *Bull. seism. Soc. Am.*, **74,** 1605–1621.

Menke, W.H. & Richards, P.G., 1980. Crust–mantle whispering gallery phase: A deterministic model of teleseismic P_n propagation, *J. geophys. Res.*, **85,** 5416–5422.

Menke, W.H. & Richards, P.G., 1983. The horizontal propagation of P waves through scattering media: Analog model studies relevant to long-range P_n propagation, *Bull. seism. Soc. Am.*, **73,** 125–142.

Molnar, P. & Oliver, J., 1969. Lateral variations of attenuation in the upper mantle and discontinuities in the lithosphere, *J. geophys. Res.*, **74,** 2648–2682.

Müller, G., 1971. Approximate treatment of elastic body waves in media with spherical symmetry, *Geophys. J. R. astr. Soc.*, **23,** 435–449.

O'Doherty, R.F. & Anstey, N.A., 1971. Reflections on amplitudes, *Geophys. Prospect.*, **19,** 430–458.

Pavlenkova, N.I. & Egorkin, A.V., 1983. Upper mantle heterogeneity in northern part of Eurasia, *Phys. Earth planet Inter.*, **33,** 180–193.

Richards, P.G. & Menke, W., 1983. The apparent attenuation of a scattered medium, *Bull. seism. Soc. Am.*, **73,** 1005–1021.

Ryberg, T., Fuchs, F., Egorkin, A.V. & Solodilov, L., 1995. Observations of high-frequency teleseismic P_n waves on the long-range Quartz profile across Northern Eurasia, *J. geophys. Res.*, **100,** 18 151–18 163.

Ryberg, T., Wenzel, J., Mechie, J., Egorkin, A.V., Fuchs, K. & Solodilov, L., 1996. 2D-Velocity structure beneath northern Eurasia derived from the super long-range seismic profile Quartz, *Bull. seism. Soc. Am.*, in press.

Sereno, T.J. & Orkutt, J.A., 1985. Synthesis of realistic oceanic P_n wave trains, *J. geophys. Res.*, **90,** 12 755–12 776.

Sereno, T.J. & Orkutt, J.A., 1987. Synthetic P_n and S_n phases in the frequency dependence of Q of oceanic lithosphere, *J. geophys. Res.*, **92,** 3541–3566.

Shapiro, S.A. & Hubral, P., 1996. Elastic waves in random multilayered structures: Equivalent dynamic medium and generalized O'Doherty–Anstey formulas, *Geophysics,* in press.

Shapiro, S.A. & Kneib, G., 1993. Seismic attenuation by scattering: theory and numerical results, *Geophys. J. Int.*, **114,** 373–391.

Shapiro, S.A., Zien, H. & Hubral, P., 1994. A generalized O'Doherty–Anstey formula for waves in finely layered-media, *Geophysics,* **59,** 1750–1762.

Stephans, C. & Isacks, B.L., 1977. Toward an understanding of S_n; Normal modes of Love waves in an oceanic structure, *Bull. seism. Soc. Am.,* **67,** 69–78.

Sutton, G.H. & Walker, D.A., 1972. Oceanic mantle phases recorded on seismographs in the northwestern Pacific at distances between 7° and 40°, *Bull. seism. Soc. Am.,* **62,** 631–655.

Wessel, P. & Smith, W.H.F., 1995. New version of the generic mapping tools (GMT) version 3.0 released, EOS, Trans. *Am. geophys. Un.,* **76,** 329.